Article

A multi-band refinement technique for analyzing electronic band structure of thermoelectric materials

Agrawal et al. report a multi-band refinement technique for analyzing the electronic band structure of thermoelectric materials. They demonstrate that the effects of temperature, doping, and alloying on the electronic band structure and scattering parameters can be easily captured by this technique.

Bharti Agrawal, Johannes de Boor, Titas Dasgupta

titas.dasgupta@iitb.ac.in

Highlights

Refinement-based approach for extracting electronic band structure information

Experimental data of electrical properties and a transport model as inputs

Applicable to semiconductors with multiple-band-dominated charge transport
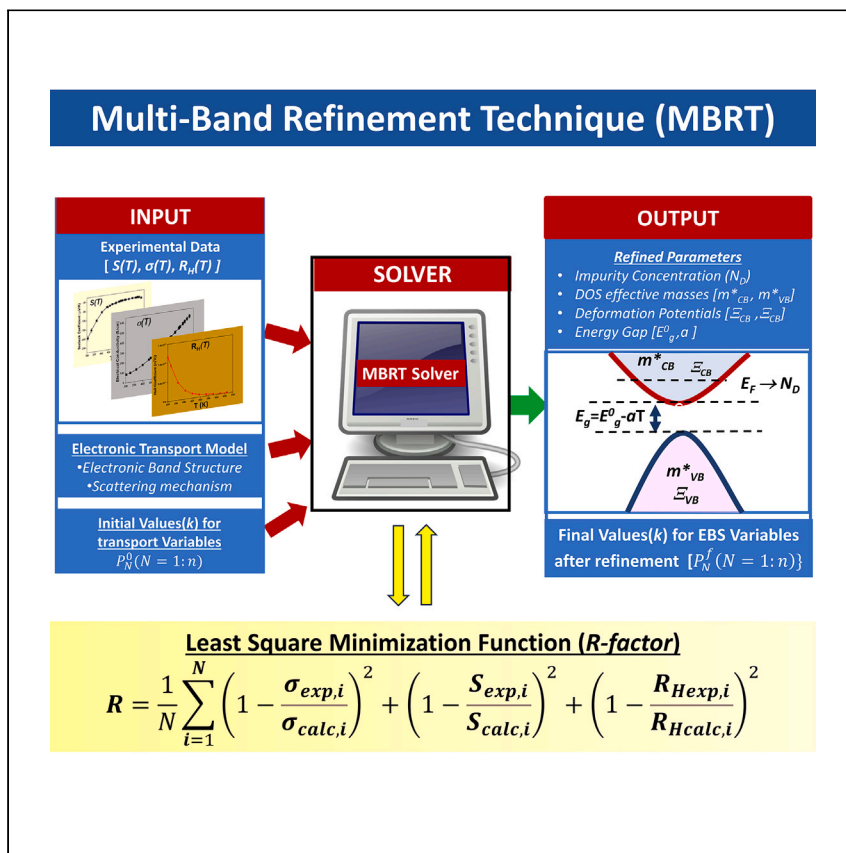
Method validated using silicon and magnesium silicide

Article

A multi-band refinement technique for analyzing electronic band structure of thermoelectric materials

Bharti Agrawal,[1] Johannes de Boor,[2,3] and Titas Dasgupta[1,4,*]

SUMMARY

Investigation of electronic band structure (EBS) plays a pivotal role in the advancement of thermoelectric materials and devices. Sophisticated experiments and theoretical calculations are required to obtain EBS information, representing a bottleneck in studying the vast and increasing number of thermoelectric materials. Herein, we propose a refinement-based approach, referred to as the multi-band refinement technique (MBRT), that combines routine laboratory measurements with computationally inexpensive calculations to acquire EBS information. Experimental data of electrical conductivity, Seebeck coefficient, and Hall coefficient along with an electronic transport model act as inputs. The MBRT solver uses this information to iteratively refine electronic structure and scattering parameters by a least-square minimization technique. The efficacy of the MBRT has been validated using silicon, an archetypal semiconductor, and Mg$_2$Si, a well-known thermoelectric material. The results demonstrate that the MBRT can be a powerful tool for studying the effects of temperature, doping, and alloying on the EBS of thermoelectric materials.

INTRODUCTION

Thermoelectric (TE) technology can be used to directly convert waste heat into electricity, making it an important avenue for renewable energy harvesting.[1,2] Discovery of efficient TE materials[3,4] can thus contribute to the reduction of fossil fuel consumption, which has a high carbon footprint. The performance of a TE material is defined by the dimensionless parameter[5]

$$zT = \frac{S^2 \sigma}{\kappa} T. \tag{Equation 1}$$

Here, S is Seebeck coefficient, σ is electrical conductivity, κ is thermal conductivity, and T is absolute temperature. These TE properties are strongly influenced by charge-transport behavior. Thus, tuning of various electronic band structure parameters (which include Fermi level position, band effective mass, band degeneracy, band gap, inter-band separations) and scattering mechanisms[5] is essential for the development of high-performance TE materials. Historically, estimation of these parameters has been done using a combination of experimental techniques like cyclotron resonance,[6–8] Shubnikov-de Haas measurement,[9] angle-resolved photoemission spectroscopy (ARPES), and UV/infrared (IR) spectroscopy.[10,11] These methods have created a wealth of information on standard semiconductors like Si, Ge, and GaAs.[12–14] However, these experiments usually require high-quality single crystals and hence can be difficult to replicate on the vast number of known TE

[1]Department of Metallurgical Engineering and Materials Science, Indian Institute of Technology Bombay, Mumbai 400 076, India

[2]Institute of Materials Research, German Aerospace Center (DLR), 51147 Cologne, Germany

[3]Faculty of Engineering, Institute of Technology for Nanostructures (NST) and CENIDE, University of Duisburg-Essen, 47057 Duisburg, Germany

[4]Lead contact

*Correspondence: titas.dasgupta@iitb.ac.in

https://doi.org/10.1016/j.xcrp.2024.101781

compounds.[15–17] Further, these are niche experiments and cannot be performed using routine laboratory equipment. Thus, in recent years, there has been a shift toward first-principles-based theoretical methods for studying the electronic band structure of TE semiconductors.[18] These *ab initio* techniques can be used to calculate the energy dispersion near the band edge at 0 K and thus provide information about bands relevant to charge transport. Recent advances also indicate accurate estimation of carrier scattering rates from first-principles calculations.[19] However, there are limitations to these techniques that include under-estimation of the band gap and accuracy in strongly correlated systems. Thermal vibration of atoms also results in changes in their interaction with the charge carriers. Thus, various parameters associated with the electronic band structure (EBS) have a temperature dependence that needs to be taken into account for the calculation of charge-transport properties. Density functional perturbation theory (DFPT)[20] can be utilized for this but is computationally expensive, thereby limiting its usage. The other problem associated with traditional *ab initio* techniques is their limited ability to handle disorder/defects, which are inherently present in all materials. Thus, TE applications, which require temperature-specific EBS information, rely on experimental transport measurements like σ, S, Hall coefficient, and Nernst coefficient.[21] The EBS information is then deconvoluted from these data using phenomenological models based on the Boltzmann transport equation.[22–24] This method has been shown to estimate and predict electronic-transport-related information in numerous TE materials, which include features of the EBS (e.g., band convergence effect,[25–29] changes in inter-band separation with temperature,[30] band-gap estimation[31]), scattering mechanism,[32–34] charge-carrier optimization and performance prediction,[35–39] and materials design.[40] However, there are drawbacks, as most of these models assume a single effective band to mimic the majority carrier transport while neglecting minority carriers. This is done to obtain a unique solution but restricts the number of parameters that can be handled. Recent studies[23,41] indicate that this can result in incorrect EBS parameters in semiconductors with complex band structures (presence of multiple valleys near the band extrema). For some materials, multi-band models have been developed.[42–46] These are, however, pointwise solutions, and the methodology for arbitrary material systems is missing. Furthermore, it has not been clarified if the employed models are indeed the best descriptions of the respective material systems.

Thus, an approach that can provide information on all EBS and scattering parameters and at the same time be obtained from routine laboratory measurements would be highly beneficial for studying TE materials. In this work, a refinement technique (referred to as the multi-band refinement technique [MBRT]) has been proposed. The MBRT method requires experimental data of electrical properties and an electronic transport model as inputs and sequentially refines the associated EBS and scattering parameters. The technique uses least-square minimization for the refinement process, which is similar to the Rietveld method.[47,48] The refinement process involves iterative adjustments in the parameters and is continued until an acceptable match is obtained between the experimental and calculated electrical properties. The advantages of this technique are that (1) the MBRT can refine multiple parameters, which is unlike existing solution-based methods. It can thus account for materials with complex band structures with multiple bands close to the band extrema. The effects of temperature, doping concentration, and alloying on the EBS can also be studied using this technique, and subtle changes can be detected. To account for these features, the temperature dependence of parameters like band gap and inter-band separation has been considered. (2) Apart from EBS information, this technique allows for extracting charge scattering information. Acoustic phonon
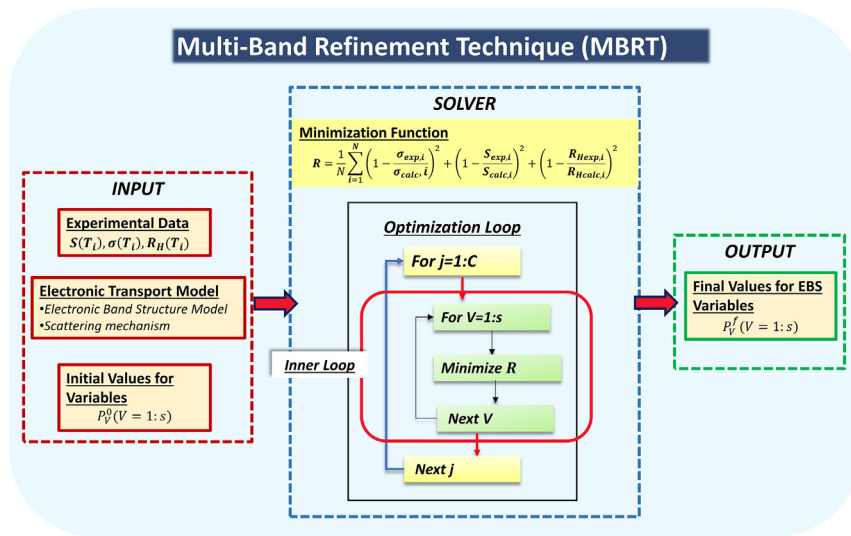
Figure 1. Block diagram representation of the multi-band refinement technique (MBRT)
The schematic represents an overview of MBRT. The set of input, i.e., experimental thermoelectric properties, electronic transport model, and initial values for variables, are mentioned in the input block, followed by the solver block presenting sequential refinement of individual variables. The output block represents the results of the MBRT, which are the refined electronic transport parameters.

scattering is considered to be the dominant scattering mechanism in TE materials at high temperatures.[24] Accordingly, the deformation potential values for individual bands can be calculated using the MBRT. Currently, grain-boundary scattering, which is relevant in many TE materials,[34,49] can also be studied. (3) The MBRT is computationally inexpensive and can be easily adopted.

The MBRT method has been tested on (1) n-type silicon, a well-known semiconductor for which EBS information is available,[12] and (2) n-type Mg_2Si, which is a state-of-the-art TE material.[50] The results from the MBRT for both Si and Mg_2Si show an excellent match of the refined parameters with literature reports, highlighting its applicability for studying TE semiconductors.

RESULTS AND DISCUSSION

Methodology

The block diagram representation of the MBRT is shown in Figure 1. Input to the model consists of (1) temperature-dependent experimental data of S ($S(T)$), σ ($\sigma(T)$), and Hall coefficient ($R_H(T)$), (2) an electronic transport model, and (3) initial values for all the variables (P_V^0). The experimental data can be obtained from standard measurements.[51–59] It is necessary to have the experimental data of $S(T_i), \sigma(T_i)$, and $R_H(T_i)$ at fixed temperature points (i = first temperature data point; last temperature data point at regular intervals). Polynomial fitting (usually of the 2nd or 3rd order) of the raw data has been done to obtain this. A uniform temperature interval of $\Delta T = 10$ K has been used in this study. The electronic transport model consists of EBS and charge-carrier scattering information specific to the given material system. The EBS model contains details regarding those energy bands that contribute to charge transport. This can be obtained from literature reports or calculated by $ab\ initio$ methods for any TE material. In the case of solid solutions, the EBS model can be inferred from the end members, assuming linear variations in the band positions and band curvatures.[26,60]

It is then important to identify the bands relevant to charge transport. This depends on the position of the Fermi level, e.g., in heavily doped TE materials, the minority bands can be neglected.[24] Similarly, at low doping or high temperatures, mixed conduction is usually relevant, hence both majority and minority bands need to be included.[42–44,46,61,62] The position of these bands in k-space can be used to obtain their valley degeneracy number (N_V). Once the EBS model is finalized, the list of variables needs to be decided. The band effective mass (m_b^*) for each band, the band gap (E_g), and the inter-band energy separations (E_i) are variables to be optimized. Since the band gap and inter-band separations are known to have a temperature dependence, a linear variation has been considered in this study that results in one additional variable per considered band.[11] The temperature-dependent changes in the inter-band separations and band gap are important to study in TE materials, as they provide vital information regarding band convergence, mixed conduction, and bipolar thermal effects. The m_b^* and deformation potentials (Ξ) can also have a temperature dependence, but the change is usually negligible compared to the temperature dependence of energy-gap parameters.[63] Considering the coupling between m_b^*, Ξ, E_g, and E_i parameters, the temperature dependence of m_b^* and Ξ has been neglected in this study. The other information required in the electronic transport model is the charge-carrier scattering mechanism.[22,64,65] For heavily doped TE materials and at high temperatures, acoustic phonon (AP) scattering is the dominant mechanism and has been considered in the study.[24] Thus, deformation potentials of the individual bands are additional variables to be refined. Other scattering mechanisms might also need to be incorporated depending on the material system and studied temperature range (e.g., in Mg_2Si, grain boundary scattering has been considered[34] in this study). In the case of multiple scattering mechanisms, the overall mobility parameter (μ_0) can be defined using Matthiessen's rule[66]: ($\mu_0 = \left(\sum \frac{1}{\mu_{0,i}} \right)^{-1}$). Here, $\mu_{0,i}$ represents the mobility expression for individual scattering mechanisms.

For each variable ($P_V, V = 1:s$), here, V represents an individual variable and s defines the total number of refinement variables. Initial guess values (P_V^0) are required and serve as the starting point for the optimization routine. Since the MBRT utilizes a least-square minimization technique, refinement of the initial guess values always leads to the closest minimum. Thus, the guess values need to be close to the global minimum. This information can be obtained for any TE material using a combination of n- and p-type heavily doped compositions. Since the minority band contributions can be neglected in heavily doped compositions and at low temperatures, information about the conduction/ valence band edge can be extracted from these compositions utilizing single-band (SPB or SKB)-based models. Further, the variation of SPB/SKB density of states (DOS) mass with carrier concentration can be used as an indicator of the presence of additional bands close to the edge, and this information can be exploited while deciding the electron transport model. Another approach to obtain initial value information of materials would be from DFT calculations on defect-free materials, which are computationally inexpensive. This can be used to obtain ground-state information of relevant bands and can act as the guess values. Literature reports of EBS parameters can be further used to supplement the data. Discussion on the guess values for the studied materials is provided in the results and discussion section and in the supplemental information (see Notes S3 and S4). This input information is fed to the MATLAB-based MBRT solver. Refinement of the variables is then performed iteratively by minimizing the difference between the experimental and calculated transport properties. A least-square minimization function[67] (R) has been defined for this purpose and is given in Table 1. In this expression, the subscripts *exp* and *calc* refer to the experimental and theoretical values, respectively. N refers to the total number of temperature points, and *i* represents

Table 1. List of equations used in the MBRT code

	Expression
Individual band (i^{th})	
Charge-carrier concentration (n_i)	$n_i = \dfrac{(2m_D^* k_B T)^{\frac{3}{2}}}{2\pi^2 \hbar^3} F_{\frac{1}{2}}(\eta)$
DOS effective mass (m_D^*)	$m_D^* = N_V^{2/3} m_b$
Electrical conductivity (σ_i)	$\sigma_i = \dfrac{8\pi e}{3h^3} \mu_0 (2m_D^* k_B T)^{\frac{3}{2}} F_0(\eta)$
Seebeck coefficient (S_i)	$S_i = \left(-\dfrac{k_B}{e}\right)\left(\dfrac{2F_1(\eta)}{F_0(\eta)} - \eta\right)$
Hall coefficient ($R_{H,i}$)	$R_{H,i} = \dfrac{3}{4}\dfrac{F_{0.5}(\eta)F_{-0.5}(\eta)}{F_0(\eta)F_0(\eta)}\dfrac{1}{n_i e}$
Multi-band	
Charge balance equation	$\sum_{i=1}^{M} n_i + N_A = \sum_{i=1}^{Q} p_i + N_D$
Electrical conductivity (σ)	$\sigma_{calc} = \sum_i^{M+Q} \sigma_i$
Seebeck coefficient (S)	$S_{calc} = \dfrac{\sum_i^{M+Q} \sigma_i S_i}{\sum_i^{M+Q} \sigma_i}$
Hall coefficient (R_H)	$R_{Hcalc} = \dfrac{\sum_i^{M+Q} R_{H,i}\sigma_i^2}{\left(\sum_i^{M+Q}\sigma_i\right)^2}$
Charge-carrier scattering mechanism	
Acoustic phonon (AP)	$\mu_{0,AP} = \dfrac{e\pi\hbar^4 d v_l^2}{\sqrt{2}\,\Xi_n^2 m_b^{*5/2}(k_B T)^{3/2}}$
Grain boundary (GB)	$\mu_{0,GB} = Le\left(\dfrac{1}{2\pi m_b^* kT}\right)^{\frac{1}{2}} e^{\left(-\frac{E_b}{kT}\right)}$
Minimization function (R factor)	$R = \dfrac{1}{N}\sum_{i=1}^{N}\left(1 - \dfrac{\sigma_{exp,i}}{\sigma_{calc,i}}\right)^2 + \left(1 - \dfrac{S_{exp,i}}{S_{calc,i}}\right)^2 + \left(1 - \dfrac{R_{Hexp,i}}{R_{Hcalc,i}}\right)^2$
Quality of refinement	R factor $\chi = \dfrac{R}{R_{exp}}$

List of equations used in the MBRT code.[6,22,24,34,43,67] i, band number; m_D^*, DOS effective mass; m_b^*, band effective mass; N_V, valley degeneracy; T, temperature; η, Fermi level; $F_j(\eta)$, Fermi integral; μ_0, free mobility; n/p, electron/hole concentration; M, number of conduction bands; Q, number of valence bands; N_A, acceptor concentration; N_D, donor concentration; *_calc, calculated data; *_exp, measured data; v_l, longitudinal velocity of sound; Ξ_n, deformation potential; d, density; E_b, grain boundary activation energy; L, average grain size; N, number of temperature points; χ, goodness of fit factor.

individual temperature points. At each temperature point, the theoretical values for the electrical properties (S, σ, R_H) are calculated. Multi-band charge-transport equations (given in Table 1) have been formulated based on the electronic transport model to obtain the theoretical values. In these equations, the individual band contributions are estimated from the Boltzmann transport equation.[68] Also, bands have been considered as parabolic and rigid with respect to temperature. AP scattering has been assumed to be the dominant charge-carrier scattering mechanism. The R factor is calculated for a set of variables using the experimental and calculated values of S, σ, and R_H at each temperature point. All the variables are sequentially optimized within each refinement cycle with guess values as starting point. In general, the number of refinement cycles (C) depends on the initial parameters and electronic transport model. In this study, a convergence limit (relative change between two consecutive R factor values) of 10^{-2} has been used.

An example of the MBRT is shown in Figure 2. A two-band (one conduction band [CB] and one valence band [VB]) EBS model and AP scattering have been taken as input. This gives a total of seven variables ($V = 1 : 7$) as shown in Figure 2A. Defining the sequence in which the different variables need to be optimized is the first step of the refinement process. This is decided based on the impact of each variable
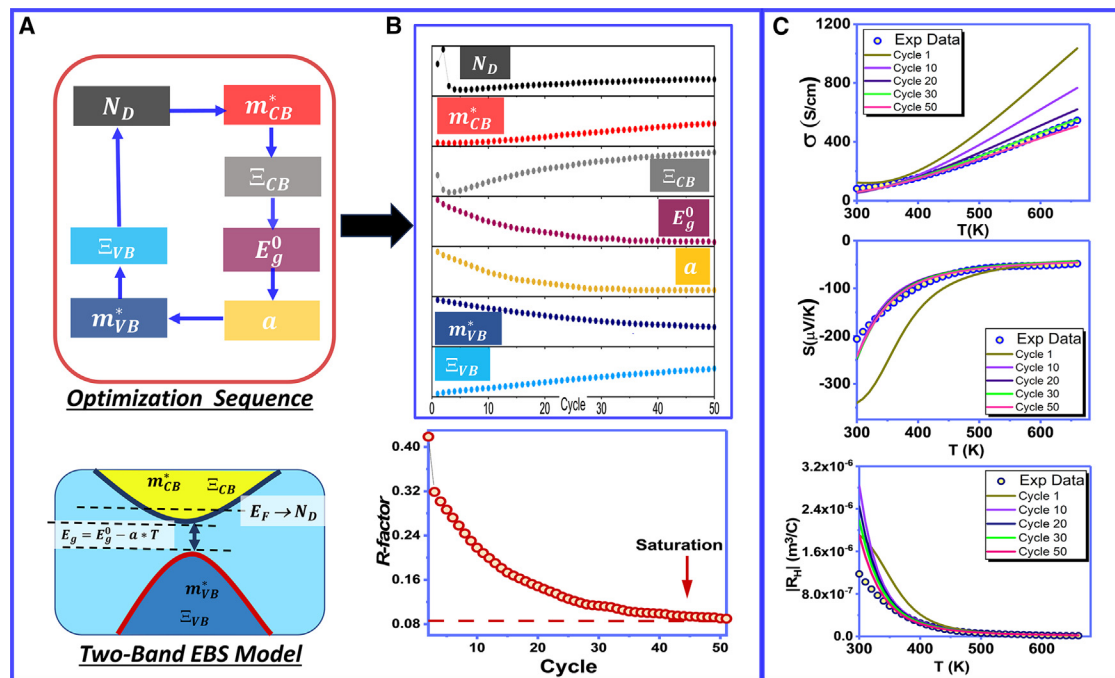
Figure 2. Illustration of processes involved during multi-band refinement

(A) The optimization sequence of the variables along with a schematic representation of a two-band EBS model (here, N_D is donor concentration; m^*_{CB} and m^*_{VB} represent the DOS effective mass of the conduction and valence bands, respectively; Ξ_{CB} and Ξ_{VB} are the corresponding deformation potentials; E_g is the band gap; E^0_g is the band gap at 0 K; a is the temperature dependence of the band gap; and E_F is the Fermi level).

(B) Top: incremental changes in the variables with the number of refinement cycles. Bottom: the corresponding R factor as a function of number of refinement cycles.

(C) Progression in the fitting quality for σ, S, and R_H, respectively, with the number of refinement cycles.

on the electrical properties. In general, the donor or acceptor concentration is always the first variable to be refined, as it regulates the position of the Fermi level. This is followed by the majority band variables, i.e., related to the CB if n-type and to the VB if p-type. Variables associated with band gap are refined after the majority band variables. Finally, the minority band variables are refined. The reason for prioritizing band-gap variables over the minority band variables is their higher influence on the TE properties. Further details regarding sequence of optimization have been discussed in the supplemental information (Notes S3 and S4; Figure S3). The example in Figure 2 is that of an n-type TE material; thus, the highest priority variables are N_D (donor concentration) and CB variables (m^*_{CB} and Ξ_{CB}). This is followed by the band-gap variables (E^0_g and a) and finally the VB variables (m^*_{VB} and Ξ_{VB}).

In Figure 2B, the changes in each variable as a function of the refinement cycle (C) is depicted. The bottom image in Figure 2B depicts the R factor, which saturates after ~50 cycles. Thus, the refinement process can be described as an incremental adjustment of the variables in each iteration step in order to lower the R factor values. In Figure 2C, the progression in the fit of all the calculated electrical properties with the number of refinement cycles is shown. The difference between experiment (hollow circle) and calculated data decreases with an increase in number of refinement cycles.

Since the MBRT method has similarities to the Rietveld refinement technique,[47,48,69] which is an established technique, a direct comparison between the two helps in

Table 2. Comparison of the MBRT and the Rietveld refinement method

	MBRT method	Rietveld method[47]
Experimental input	electrical properties ($S(T), \sigma(T), R_H(T)$)	diffraction data (intensity vs. 2θ)
Structural model	electronic band structure (EBS) and charge-carrier scattering information	crystal structure information
Minimization function	$R = \frac{1}{\theta_N} \sum_{i=1}^{\theta_N} \left(1 - \frac{\sigma_{exp,i}}{\sigma_{calc,i}}\right)^2 + \left(1 - \frac{S_{exp,i}}{S_{calc,i}}\right)^2 + \left(1 - \frac{R_{Hexp,i}}{R_{Hcalc,i}}\right)^2$	$\sum_i w_i (y_i^{obs} - y_i^{calc})^2$
Constitutive equations	BTE-based multi-band equations (given in Table 1)	$y_{ic} = y_{ib} + \sum_\varphi S_\varphi \sum_k G_\varphi(2\theta_i - 2\theta_k) I_k$ $I_k = m_k L_k \lvert F_k \rvert^2 P_k A_k$
Refined variables	band-structure parameters: band effective mass, band gap, inter-band separation, scattering terms (deformation potential, alloy scattering potential, grain boundary energy, etc.)	crystal structure parameters: lattice constant, atomic position, occupancy, thermal displacement parameter, etc.
Quality of refinement	*R factor* and goodness-of-fit factor (χ)	$R_{wp} = \left[\dfrac{\sum_i w_i (y_i^{obs} - y_i^{calc})^2}{\sum_i w_i (y_i^{obs})^2}\right]^{1/2}$, $\chi^2 = \dfrac{R_{wp}}{R_{exp}}$

understanding its capabilities and limitations. In Table 2, the analogies between the two methods have been presented. As seen from the table, both methods rely on experimental data and a structural model as inputs. Also, the minimization functions are based on the least-square error (*LSE*) method. The critical requirement during Rietveld refinement is to prevent the minimization function from settling at a local minimum. This is done by a sequential refinement of various crystal structure parameters. Similarly, avoiding false minima during MBRT refinement is crucial to identify the correct EBS variables. A sequential refinement of the EBS variables based on their impact on the transport data has been adopted to overcome this problem. Finally, the quality of refinement in the Rietveld method is quantified using cost functions (R_{wp} factor and χ^2 are listed in Table 2). In the MBRT method, the quality of refinement is defined by the *R factor*, which is mathematically similar to the R_{wp} factor. In addition, the goodness of fit (GoF) parameter $\chi = \frac{R}{R_{exp}}$ has been defined, where R_{exp} is a measure of the ideal *R factor* and is defined by

$$R_{exp} = (\delta\sigma)^2 + (u\sigma)^2 + (\delta S)^2 + (uS)^2 + (\delta R_H)^2 + (uR_H)^2 \qquad \text{. (Equation 2)}$$

In this equation, the prefixes "δ" and "u" refer to the relative precision and accuracy of the measurement instruments, respectively. An R_{exp} value of 0.0271 is obtained based on the uncertainties in the measurements used in this study. The GoF parameter (χ) defines the quality of refinement. χ values much larger than unity indicate false minima or an incorrect EBS model or scattering mechanism. Details about the quality of refinement are provided in Note S2 and Table S1.

The applicability of the MBRT method was tested on elemental silicon and n-type Mg_2Si compositions. Silicon was chosen due to the availability of a vast amount of literature on its EBS.[12,45,64,70–74] This provides the ideal platform for validation of the obtained refined variables. n-Type Mg_2Si compositions, a low-cost TE material, have been studied by the MBRT due to their potential application in TE devices.[36,50,75,76] Details of the obtained results are provided in this section.

Silicon wafer

A commercial phosphorus-doped silicon wafer (Wafer World, grade: prime, dopant: phosphorus) was used for this study. The data obtained from polynomial fitting of
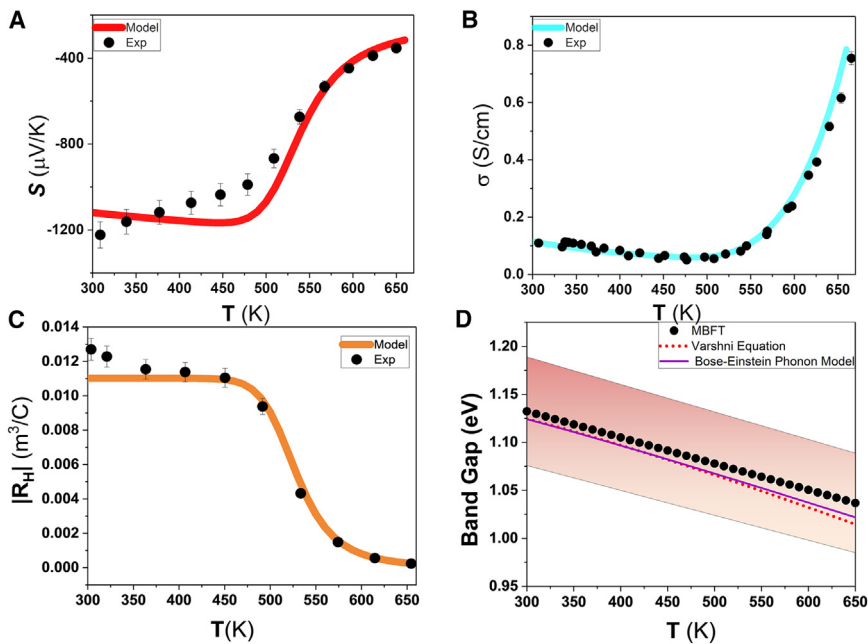
Figure 3. Multi-band refinement results for n-type low-doped silicon wafer

(A–C) Comparison of the experimental (Exp) and calculated data (Model) of R_H, σ, and S as a function of temperature, with error bars representing 5%, 3%, and 5% measurement uncertainties, respectively.

(D) The estimated band-gap values are compared with literature models. The shaded region indicates a $\pm 5\%$ error bar of the measurement uncertainty.

the experimental measurements $S(T)$, $\sigma(T)$, and $R_H(T)$ have been used as inputs to the solver (see Figure S2). A two-band model consisting of a single CB and a single VB was used as the input EBS model for the solver. The initial values for the variables were taken from literature and are provided in Table S2. In Figures 3A–3C, the calculated R_H, σ, and S data, along with the experimental data, are plotted (details of the EBS models, guess values, and optimization process are provided in Note S3; Figure S4 explains the cause of mismatch in R_H and S data near room temperature). An *R factor* value of 0.0226 was obtained after saturation. The refined EBS variables are given in Table 3 along with literature reports.

The obtained DOS effective masses (m^*_{CB}, m^*_{VB}) are within ~10% of that obtained from cyclotron measurements. Similarly, the deformation potential values (Ξ_{CB}, Ξ_{VB}) have a similar deviation (~10%) compared to DFPT[79] calculations. It is to be noted that for materials with anisotropic band masses, the effective anisotropy parameter (K^*)[80] needs to be considered while utilizing the mobility expressions, as the inertial effective mass (m_I) can no longer be considered the same as the band mass (m^*_b). The K^* value can be obtained from the anisotropy parameter ($m^*_{\parallel}/m^*_{\perp}$) as suggested by Gibbs et al.[80] The other refined variables (E^0_g, a) related to the band gap are also close to reported experimental data. In Figure 3D, the temperature variation of the estimated band gap in silicon is plotted along with literature reports (obtained from Varshni's formula and the Bose-Einstein phonon model, including optical phonons). The shaded region indicates a range of $\pm 5\%$.

Overall, all the refined variables converge to values close to literature reports, indicating the efficacy of the MBRT method. The deviations in the refined values lie between 3% and 12% and reflect the cumulative effect of various error sources. These include errors due to deficiencies in the starting EBS model, proximity of initial guess

Table 3. Comparison of the refined EBS variables for silicon with literature reports

EBS variable	This work (MBRT)	Literature	δ (%)
$m^*_{CB}(/m_0)$ (CB DOS effective mass)	1.36	1.19 (cyclotron measurement)[12]	12.5
		1.14 (DFT calculation with HSE06 xc)[77]	16.1
		1.40 (two-band model)[45]	2.9
Ξ_{CB} (eV) (deformation potential CB)	9.32	9.0 (ToF data with Monte Carlo)[78]	3.4
		8.21 (DFPT calculation with PBE xc)[79]	11.9
$m^*_{VB}(/m_0)$ (VB DOS effective mass)	0.74	0.81 (cyclotron measurement)[12]	9.4
Ξ_{VB} (eV) (deformation potential VB)	5.80	5.48 (DFPT calculation with PBE xc)[79]	5.5
E^0_g (eV) (band gap at 0 K)	1.21	1.17 (experiment)[12]	3.3
		1.08 (DFT calculation with HSE06 xc)[77]	10.7
		1.13 (two-band model)[45]	6.6
a (eV /K) (temperature dependence of band gap)	0.000273	0.000316 (Varshni model[a])[12]	15.7
		0.000293 (Bose-Einstein phonon model[a])[74]	7.3

δ indicates the percentage of deviation of the data from literature.
[a]Calculated assuming a linear temperature dependence.

values, and errors in the measured experimental data.[51–59] In Figure 4A, the influence of the proximity of the guess value (referred to as δ [starting value]) on the refined values is shown for the different variables (δ [refined value]). The variables shown in Figure 4A have been categorized depending on the extent of deviation in the refined value. N_D and E^0_g, which have the least errors, are marked by solid lines, and these variables converge to the final values even when the guess values deviate significantly (up to ±30%). At the other extreme are the minority band variables (m^*_{VB}, Ξ_{VB}) (shown by dashed lines), which can have significant errors in the final values depending on the starting position. The errors in the majority band variables (m^*_{CB}, Ξ_{CB}) (shown by solid lines with symbols) lie in between. It is to be noted that these calculations were performed considering uniform deviation of the guess values for all the variables. The errors can be reduced significantly for non-uniform deviations (only m^*_{VB} and Ξ_{VB} were deviated), as shown in the inset of Figure 4A. Thus, it can be inferred that (1) starting with initial values that are close to the final ones is important to avoid false minima, (2) variables for minority carriers are more sensitive, which reflects their lower contribution in the experimental data, and (3) a sequential approach to the refinement is the best option to reach the global minimum.

The other source of error in the data originates from inaccuracies in the measured data. The associated uncertainties are difficult to extract in a multi-band scenario due to the unavailability of analytical expressions. However, rough estimates can be obtained from reported single-band expressions. In Figure 4B, the fractional uncertainty in m^*_D has been estimated using Snyder's expression[81]:

$$m^*_s = \frac{h^2}{2k_B T}\left(\frac{3n_H}{16\sqrt{\pi}}\right)^{2/3}\left[\frac{\left(exp\left[\frac{|S|}{k_B/e} - 2\right] - 0.17\right)^{2/3}}{1+exp\left[-5\left(\frac{|S|}{k_B/e} - \frac{k_B/e}{|S|}\right)\right]} + \frac{\frac{3}{\pi^2}\left(\frac{2}{\sqrt{\pi}}\right)^{2/3}\frac{|S|}{k_B/e}}{1+exp\left[5\left(\frac{|S|}{k_B/e} - \frac{k_B/e}{|S|}\right)\right]}\right]$$

(Equation 3)

Here, m^*_s is defined as the Seebeck effective mass with $m^*_s = m^*_D$ for AP scattering and n_H represents the Hall carrier concentration.[24] The data indicate variations between 3% and 8% due to instrumental errors. Similarly an estimate of the uncertainty in the band-gap value can be obtained from the Goldsmid expression[82]($E_g = 2S_{max}T_{max}$),
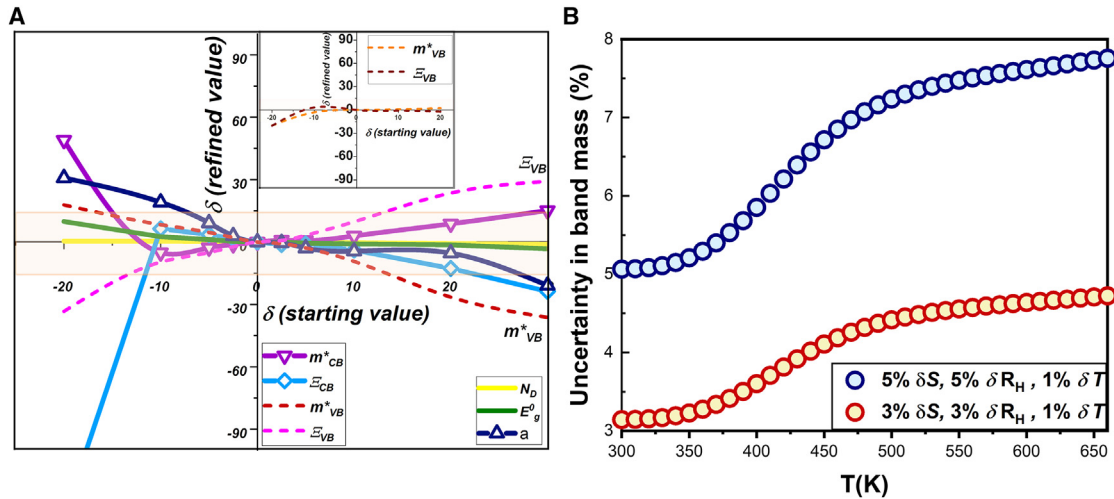
Figure 4. Uncertainty analysis of MBRT

(A) The effect of deviation of the guess values on the error in the final data (inset shows the errors in m^*_{VB} and Ξ_{VB} when the other variables have no errors). The shaded region indicates an error of $\pm 15\%$.

(B) The fractional uncertainty in the density of states mass ($\delta m^*_D / m^*_D$) as a function of temperature for two different combinations of errors in S, R_H, and T.

which yields deviations between 4% and 6% ($\delta S = 3\%, 5\%, \delta T = 1\%$). Comparing these values with the deviations obtained in Table 3, it can be inferred that instrumental uncertainties are the major contributors to the obtained δ values.

Mg₂Si compounds

Polycrystalline compositions of n-type $Mg_{2.2}Si_{1-x}Bi_x$ (x = 0.0, 0.005, 0.01, 0.02) were prepared for this study and experimental data of $S(T), \sigma(T)$ and $R_H(T)$ were collected between 300 K and 660 K (data provided in Figure 5). Polynomial fitting of the TE data is shown in Figure S5. Reported ground-state EBS calculations indicate that the CB edge consists of two bands (denoted here as *CB1* and *CB2*).[50] Both these bands are centered around the *X* k-point and are separated by an energy difference of $\sim$0.2–0.4 eV. The VB edge in Mg_2Si is similar to that of silicon and consists of three bands (heavy hole, light hole, and the split-off band). Since all the studied compositions were n-type, these bands were approximated by a single effective band (denoted by *VB*). The input EBS model therefore consisted of two bands (*CB1* and *VB*) for the undoped composition (x = 0) and three bands (*CB1, CB2*, and *VB*) for all the doped compositions. The rationale behind considering only two bands for the undoped composition is the large inter-band separation (E_1) between *CB1* and *CB2*. The measured σ data (shown in Figure 5 (d)) indicates a non-monotonous temperature variation. This has been attributed to resistive grain boundaries (*GBs*), which hinder charge flow at lower temperatures. To account for this, an additional contribution ($\mu_{0,GB}$) to the overall mobility (μ_0) has been considered. The analytical expression provided by Seto[83] ($\mu_{0,GB} = Le\left(\frac{1}{2\pi m^*_s kT}\right)^{\frac{1}{2}}e^{\left(-\frac{E_b}{kT}\right)}$) is used to model the *GB* contribution. Here, E_b represents the *GB* activation energy, while L represents the average grain size. The *AP* scattering and the *GB* scattering were assumed to be independent processes, and thus the total contribution can be obtained from Matthiessen's rule[66] ($\mu_0 = \left(\frac{1}{\mu_{0,AP}} + \frac{1}{\mu_{0,GB}}\right)^{-1}$). In total, there are nine variables that have been refined for both the two-band and the three-band model (Tables S4 and S5). The initial values for all the variables were taken from literature reports. Details regarding the electron transport model and guess values are provided in Note S4.
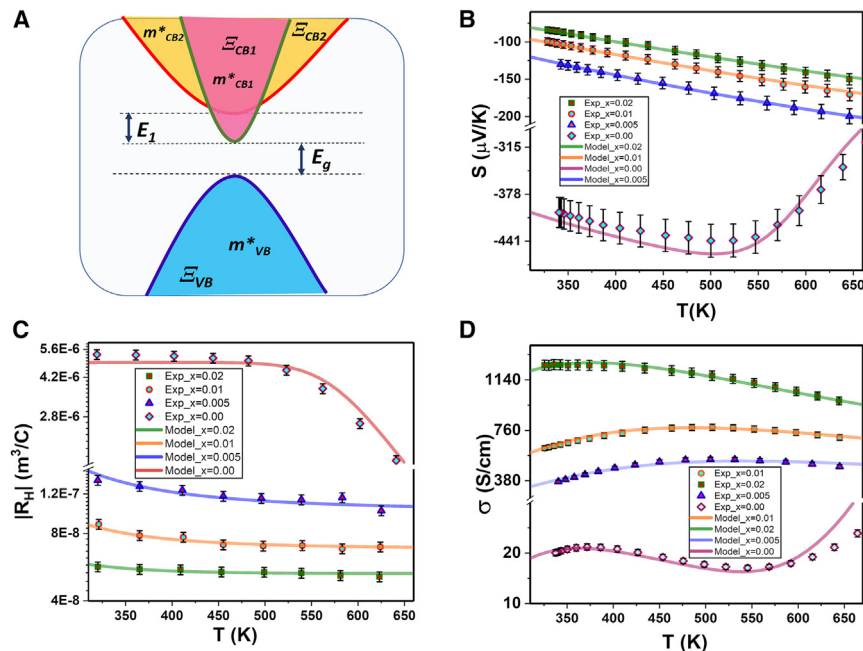
Figure 5. Multi-band refinement of n-type Mg$_2$Si

(A) EBS schematic for n-type Mg$_2$Si.

(B–D) Temperature dependence of S, R_H, and σ for all the compositions of Mg$_{2.2}$Si$_{1-x}$Bi$_x$ with x = 0.00, 0.005, 0.01, 0.02. Solid lines represent the modeled data, while symbols indicate experimental measurements. Error bars represent 5%, 5%, and 3% measurement uncertainties in S, R_H, and σ, respectively.

Initially, the undoped composition is refined. This is followed by the (individual) refinement of the doped compositions, in which the VB and band-gap (m^*_{VB}, Ξ_{VB}, E_g^0, a) parameters are taken from the refined undoped data (details about the optimization sequence and refinement process are in Note S4). In Table 4, the refined data for all the variables along with literature reports are given. The modeled S, σ, and R_H data for all the compositions are provided in Figure 5. As seen from the figure, the modeled data are in close agreement with the experimental data. This is also indicated from the obtained *R factor* (0.00078–0.012) and GoF (χ) values (0.029–0.044) (see Table S6).

The refined variables match well with literature reports (given in Table 4). Of specific note are the m^*_{VB} and E_1^0 values, for which a huge discrepancy is reported between experimental and DFT data.[89,90] Our results suggest values that are closer to DFT reports. Further, the band-gap value (E_g^0) agrees with experimental reports. A comparison of the lower CB (*CB1*) properties as a function of doping content (for which extensive literature reports exist[50]) has been carried out. Data provided in Table S5 and Figure S6 indicate no systematic variation of m^*_{CB1} with Bi doping content (mean value: 0.80 m_0, standard deviation: 0.05 m_0). This is in accordance with literature reports, where variations between 0.6 and 1.4 m_0 has been reported. Thus, both literature reports and the MBRT results indicate a rigid lower CB with Bi doping. The MBRT data of the deformation potential have a mean value of 18.4 eV and a standard deviation of 0.8 eV; however, no systematic variation of Ξ_{CB1} with N_D is observed. While no such studies are reported in literature, the small scatter in the data (~4.5%) and no systematic variation can be taken to be a signature of a rigid CB (*CB1*) with Bi doping in the Mg$_2$Si system.

Table 4. Band structure parameters of Mg$_2$Si, obtained from the MBRT along with reported theoretical and experimental data

EBS Variablevariable	This Work work (MBRT)	Literature
$m^*_{CB1}(/m_0)$ (CB1 DOS effective mass)	0.76–0.79	0.73 (DFT)[84]
		0.6–1.433 (SPB data)[50]
Ξ_{CB1} (eV) (deformation potential CB1)	17.2–18.8	15–17 (SPB data)[42,85]
$m^*_{CB2}(/m_0)$ (CB2 DOS effective mass)	1.06–1.31	1.41 (k.p. method)[86]
		0.62 (LDA data)[87]
Ξ_{CB2} (eV) (deformation potential CB2)	9.09–10.63	9.51 (multi-band fitting)[87]
$m^*_{VB}(/m_0)$ (VB DOS effective mass)	1.79	1.83 (DFT)[88]
		4 (SPB)[89]
Ξ_{VB} (eV) (deformation potential VB)	10.39	9 (SPB data)[39]
E^0_g (eV) (band gap at 0K)	0.84	0.7–0.8 (IR data)[90]
		0.78 (Hall and conductivity data)[91]
a (eV /K) (temperature dependence of band gap)	−0.000615	−0.0005 (IR data)[90]
E^0_1 (eV) (inter-band separation at 0 K)	0.14–0.15	0.21–0.26 (DFT)[86]
		0.4 (IR data)[90]
d_1 (eV /K) (temperature dependence of inter-band separation)	1.0–1.6×10^{-4}	0.89×10^{-5} (fitting of two-CB Kane model)[87]
E_b (eV) (GB activation energy)	0.05–0.13	0.095 (SPB data)[34]
L (m) (average grain size)	0.5×10^{-7}–1.7×10^{-6}	N/A

Overall, the MBRT method is shown to provide accurate EBS variables for the studied Mg$_2$Si compositions (see Table S5). A point to note is that individual Mg$_2$Si compositions were refined independently and still provide similar optimized values for different variables. This can be interpreted as a validation of the ability of MBRT to provide accurate band-structure-related information.

The MBRT is thus a powerful method for temperature- and doping-dependent EBS studies, with the only requirements being accurate electronic transport model, experimental data, and initial values for each refined variable. The use of this technique is manifold: first, it allows the extraction of microscopic material parameters, which are more fundamental than individual transport properties. EBS information are building blocks to improve the performance of all semiconductor devices in general. The MBRT can thus be an efficient technique to obtain, e.g., band-gap behavior, which is a key factor in determining the performance of devices like TE generators, solar cells, lasers, and opto-electronics. Second, the impact of various strategies like alloying, doping, and process engineering on TE performance can also be understood and used to tune the EBS in a more profound manner using this technique. Third, this technique can be used as a predictive tool[39,92,93] for materials discovery. Material parameters (B, B^*), which are defined using intrinsic material properties, have been successfully used in the past for prediction of optimal doping concentrations. The output from the MBRT can be used directly in these parameters as discussed in the supplemental information (see Note S5). An alternate approach for using the MBRT as a search tool has been suggested by Kamila et al.[39] The multi-band information from the MBRT can be utilized in place of SPB data to generate carrier-concentration- and composition-dependent 3D performance maps. Fourth, temperature-dependent EBS information can be used to model behavior of TE generators that operate under large temperature gradients and can help enhance the conversion efficiency. Our results also highlight the important role played by the initial guess values in reaching the global minimum. Thus, methods for identifying these guess values require investigation and would be beneficial to make the MBRT an even more robust tool for TE research.

The refined EBS results obtained for Mg_2Si and silicon show the utility of the MBRT. Consistency of EBS parameters with the existing literature proves the validity of the MBRT. In addition, the efficiency of this technique in terms of execution time (can be performed on a standard desktop PC; 1.6 GHz 4 Core CPU, 8 GB RAM) makes it a readily accessible tool that would enable users to study the vast number of TE compounds. Thus, the manifold benefits of the MBRT make it a prominent technique for probing the EBS and for accelerating the discovery of high-performance TE materials.

EXPERIMENTAL PROCEDURES

Resource availability

Lead contact

Further information and requests for resources should be directed to and will be fulfilled by the lead contact, Dr. Titas Dasgupta (titas.dasgupta@iitb.ac.in).

Materials availability

This study did not generate new unique reagents.

Data and code availability

All original code has been deposited at Zenodo under https://doi.org/10.5281/zenodo.10286334 and is publicly available as of the date of publication. Sample datasets and readme files have been deposited at Release v.1.0 TitasDasgupta/MBRT-Codes (github.com) under https://doi.org/10.5281/zenodo.10286334 and are publicly available as of the date of publication. Any additional information required to reanalyze the data reported in this paper is available from the lead contact upon request.

Sample preparation

Silicon

The MBRT study on silicon was performed using a commercial n-type Si wafer (Wafer World, grade: prime, dopant: phosphorus, resistivity: 1–20 Ωcm). A rectangular sample of the dimension 10 × 10 mm was precision cut with a diamond scriber and used for the electrical measurements.

Mg_2Si

Bi-doped Mg_2Si (n-type) was prepared by a two-step process of induction melting followed by hot pressing. Nominal compositions of $Mg_{2.2}Si_{1-x}Bi_x$ (x = 0.00, 0.005, 0.01, 0.02) were prepared for this study. Mg coarse powder (99.9%; SRL), Si lump (99.9999%, Alfa Aesar), and Bi pieces (99.9% Loba Chemie) were used as precursors. 10% excess Mg was taken to compensate for the Mg loss. Mg coarse powder was cold compacted before induction melting. All the precursors (Mg green pellet, Si lumps, and Bi pieces) were taken as per stoichiometry in a boron nitride (BN)-coated graphite crucible. The mixture was then melted in an atmosphere-controlled induction furnace. Melting was done at 1,090°C for 5 min in Ar atmosphere (0.5 atm).[94–96] The obtained ingot was then hand crushed in an agate mortar and pestle for around 10 min to obtain a fine powder. The powder thus obtained was placed inside a 12.7 mm diameter graphite die and hot pressed for 5 min at 870°C in Ar atmosphere at 60 MPa uniaxial pressure in the compaction cum sintering induction furnace setup. The obtained pellets were then hand polished using different grades of emery paper and used for the measurements.

Phase identification

The X-ray diffraction (XRD) pattern was recorded on the hot-pressed pellets using a PAN analytical setup with Cu Kα radiation (λ = 1.54060 Å). The indexed XRD patterns of all the compositions (x = 0.00, 0.005, 0.01, 0.02) are provided in Figure S1. Major reflections in all the compositions represent the standard Mg_2Si anti-fluorite structure (space group: Fm-3m), confirmed with the ICDD 00-001-1192 database. The presence of a secondary MgO impurity phase was also detected around 2θ = 43° in all the compositions, as is typically obtained during the synthesis of Mg_2Si.[34,94]

TE property measurements

The temperature-dependent R_H, S, and σ were measured with the help of custom-built setups in the temperature range 300–670 K. The same sample was used for all the measurements to eradicate errors due to sample inhomogeneities. Also, the same sequence of measurement (S/σ followed by R_H) was maintained in all samples. For the S/σ measurements, data were collected during both heating and cooling thermal cycles. The cooling cycle data of S/σ along with the heating cycle data of R_H were used for the MBRT analysis. This was done to minimize errors associated with changes in the samples during thermal cycling.

The van der Pauw geometry[51,97] was used for the measurement of the DC-R_H of the disc-shape sample. A magnetic field was applied across the sample in the range of $\pm$ 0.7 tesla. The current, passed perpendicular to the direction of magnetic field, was in the range 0.1–0.3 A depending on the carrier concentration. A fast reversal of the current direction and averaging of the Hall voltages were carried out to overcome the errors associated with the Peltier effect. The temperature-dependent σ and S were measured sequentially in the same measurement cycle using an in-house-developed setup.[56] The van der Pauw four-probe method and the slope method[98,99] were used for the measurements of σ and S, respectively (see room temperature data in Table S3).

Theoretical calculations

All the calculations associated with MBRT solver were performed using MATLAB software. A standard Lab desktop with 1.6 GHz, 4 Core CPU, and 8 GB RAM configuration was used. In general, it took 5–6 h for one complete run. The duration of refinement also depended on the number of parameters and the number of refinement cycles.

AUTHOR CONTRIBUTIONS

Conceptualization, B.A., J.d.B., and T.D.; methodology, B.A. and T.D.; software, B.A.; validation, B.A.; formal analysis, B.A., J.d.B., and T.D.; investigation, B.A.;

writing – original draft, B.A.; writing – review & editing, B.A., J.d.B., and T.D.; visualization, B.A. and T.D.; supervision, T.D.; funding acquisition, T.D.

DECLARATION OF INTERESTS

The authors declare no competing interests.

REFERENCES

1. Bell, L.E. (2008). Cooling, Heating, Generating Power, and Recovering Waste Heat with Thermoelectric Systems. Science *321*, 1457–1461.

2. Kajikawa, T. (2005). Thermoelectric Power Generation System Recovering Industrial Waste Heat. In Thermoelectrics Handbook (CRC Press), pp. 50–51.

3. Perumal, S., Samanta, M., Ghosh, T., Shenoy, U.S., Bohra, A.K., Bhattacharya, S., Singh, A., Waghmare, U.V., and Biswas, K. (2019). Realization of High Thermoelectric Figure of Merit in GeTe by Complementary Co-doping of Bi and In. Joule *3*, 2565–2580.

4. Liu, Z., Sato, N., Gao, W., Yubuta, K., Kawamoto, N., Mitome, M., Kurashima, K., Owada, Y., Nagase, K., Lee, C.H., et al. (2021). Demonstration of ultrahigh thermoelectric efficiency of ∼7.3% in Mg3Sb2/MgAgSb module for low-temperature energy harvesting. Joule *5*, 1196–1208.

5. Snyder, G.J., and Toberer, E.S. (2008). Complex thermoelectric materials. Nat. Mater. *7*, 105–114.

6. Dresselhaus, G., Kip, A.F., and Kittel, C. (1955). Cyclotron resonance of electrons and holes in silicon and germanium crystals. Phys. Rev. *98*, 368–384.

7. Dexter, R.N., Zeiger, H.J., and Lax, B. (1956). Cyclotron Resonance Experiments in Silicon and Germanium. Phys. Rev. *104*, 637–644.

8. Ashcroft, N.W., Mermin, N.D., and Wei, D. (2016). Solid State Physics, 2nd ed. (Cengage Learning).

9. SEILER, D.G., and STEPHENS, A.E. (1991). The Shubnikov–de Haas Effect in Semiconductors: A Comprehensive Review of Experimental Aspects. In Modern Problems in Condensed Matter Sciences (Elsevier), pp. 1031–1133.

10. Pankove, J.I. (1975). Optical Processes in Semiconductors (Dover Publications, Inc.).

11. Ravich, Y.I., Efimova, B.A., and Smirnov, I.A. (1970). In Semiconducting Lead Chalcogenides, L.S. Stil'bans, ed. (Springer US).

12. Levinshtein, M., Rumyantsev, S., and Shur, M. (1996). Handbook Series on Semiconductor Parameters (WORLD SCIENTIFIC).

13. Kim, S., Lee, M., Hong, C., Yoon, Y., An, H., Lee, D., Jeong, W., Yoo, D., Kang, Y., Youn, Y., and Han, S. (2020). A band-gap database for semiconducting inorganic materials calculated with hybrid functional. Sci. Data *7*, 387.

14. Jain, A., Hautier, G., Moore, C.J., Ping Ong, S., Fischer, C.C., Mueller, T., Persson, K.A., and Ceder, G. (2011). A high-throughput infrastructure for density functional theory calculations. Comput. Mater. Sci. *50*, 2295–2310.

15. Capper, P. (2017). Bulk Crystal Growth: Methods and Materials (Springer).

16. Zharikov, E.V. (2012). Problems and recent advances in melt crystal growth technology. J. Cryst. Growth *360*, 146–154.

17. Scheel, H.J. (2000). Historical aspects of crystal growth technology. J. Cryst. Growth *211*, 1–12.

18. Kaxiras, E. (2003). Atomic and Electronic Structure of Solids (Cambridge University Press).

19. Ganose, A.M., Park, J., Faghaninia, A., Woods-Robinson, R., Persson, K.A., and Jain, A. (2021). Efficient calculation of carrier scattering rates from first principles. Nat. Commun. *121*. 2222–9.

20. Querales-Flores, J.D., Cao, J., Fahy, S., and Savić, I. (2019). Temperature effects on the electronic band structure of PbTe from first principles. Phys. Rev. Mater. *3*. 055405.

21. Heremans, J.P., Thrush, C.M., and Morelli, D.T. (2004). Thermopower enhancement in lead telluride nanostructures. Phys. Rev. B - Condens. Matter Mater. Phys. *70*, 115334.

22. Fistul', V.I. (1969). Transport Phenomena in Heavily Doped Semiconductors. In Heavily Doped Semiconductors (Springer), pp. 77–205.

23. Naithani, H., and Dasgupta, T. (2020). Critical Analysis of Single Band Modeling of Thermoelectric Materials. ACS Appl. Energy Mater. *3*, 2200–2213.

24. May, A.F., and Snyder, G.J. (2012). Introduction to Modeling Thermoelectric Transport at High Temperatures. In Materials, Preparation, and Characterization in Thermoelectrics, D.M. Rowe, ed. (CRC Press).

25. Liu, W., Chi, H., Sun, H., Zhang, Q., Yin, K., Tang, X., Zhang, Q., and Uher, C. (2014). Advanced thermoelectrics governed by a single parabolic band: Mg 2 Si 0.3 Sn 0.7 , a canonical example. Phys. Chem. Chem. Phys. *16*, 6893–6897.

26. Liu, W., Tan, X., Yin, K., Liu, H., Tang, X., Shi, J., Zhang, Q., and Uher, C. (2012). Convergence of Conduction Bands as a Means of Enhancing Thermoelectric Performance of n -Type Mg2Si1−Snx Solid Solutions. Phys. Rev. Lett. *108*, 166601.

27. Pei, Y., Shi, X., Lalonde, A., Wang, H., Chen, L., and Snyder, G.J. (2011). Convergence of electronic bands for high performance bulk thermoelectrics. Nat. *473*, 66–69.

28. Tang, Y., Gibbs, Z.M., Agapito, L.A., Li, G., Kim, H.-S., Nardelli, M.B., Curtarolo, S., and Snyder, G.J. (2015). Convergence of multi-valley bands as the electronic origin of high thermoelectric performance in CoSb3 skutterudites. Nat. Mater. *14*, 1223–1228.

29. Zhang, J., Song, L., Pedersen, S.H., Yin, H., Hung, L.T., and Iversen, B.B. (2017). Discovery of high-performance low-cost n-type Mg3Sb2-based thermoelectric materials with multi-valley conduction bands. Nat. Commun. *8*, 13901–13908.

30. Jaworski, C.M., Nielsen, M.D., Wang, H., Girard, S.N., Cai, W., Porter, W.D., Kanatzidis, M.G., and Heremans, J.P. (2013). Valence-band structure of highly efficient p-type thermoelectric PbTe-PbS alloys. Phys. Rev. B *87*. 045203.

31. Gibbs, Z.M., Kim, H.-S., Wang, H., and Snyder, G.J. (2015). Band gap estimation from temperature dependent Seebeck measurement—Deviations from the 2e|S| maxTmax relation. Appl. Phys. Lett. *106*.

32. Wang, H., LaLonde, A.D., Pei, Y., and Snyder, G.J. (2013). The Criteria for Beneficial Disorder in Thermoelectric Solid Solutions. Adv. Funct. Mater. *23*, 1586–1596.

33. Kuo, J.J., Kang, S.D., Imasato, K., Tamaki, H., Ohno, S., Kanno, T., and Snyder, G.J. (2018). Grain boundary dominated charge transport in Mg 3 Sb 2-based compounds. Energy Environ. Sci. *11*, 429–434.

34. de Boor, J., Dasgupta, T., Kolb, H., Compere, C., Kelm, K., and Mueller, E. (2014). Microstructural effects on thermoelectric efficiency: A case study on magnesium silicide. Acta Mater. *77*, 68–75.

35. Biswas, R., Patro, P.K., and Dasgupta, T. (2022). Enhanced Thermoelectric Performance in Zn 1– x Cd x Sb (x = 0–0.375) Solid Solutions by Dynamic Optimization of Charge Carrier Concentration. ACS Appl. Energy Mater. *5*, 12752–12759.

36. Zhao, L.-D., Tan, G., Hao, S., He, J., Pei, Y., Chi, H., Wang, H., Gong, S., Xu, H., Dravid, V.P., et al. (2016). Ultrahigh power factor and thermoelectric performance in hole-doped single-crystal SnSe. Science *351*, 141–144.

37. Novitskii, A., Serhiienko, I., Novikov, S., Ashim, Y., Zheleznyi, M., Kuskov, K., Pankratova, D., Konstantinov, P., Voronin, A., Tretiakov, O.A., et al. (2022). Influence of Bi Substitution with Rare-Earth Elements on the Transport Properties of BiCuSeO Oxyselenides. ACS Appl. Energy Mater. *5*, 7830–7841.

38. Pei, Y., May, A.F., and Snyder, G.J. (2011). Self-Tuning the Carrier Concentration of PbTe/Ag2Te Composites with Excess Ag for High Thermoelectric Performance. Adv. Energy Mater. *1*, 291–296.

39. Kamila, H., Sahu, P., Sankhla, A., Yasseri, M., Pham, H.-N., Dasgupta, T., Mueller, E., and de Boor, J. (2019). Analyzing transport properties of p-type Mg 2 Si–Mg 2 Sn solid solutions: optimization of thermoelectric performance and insight into the electronic band structure. J. Mater. Chem. A *7*, 1045–1054.

40. Toberer, E.S., May, A.F., and Snyder, G.J. (2010). Zintl Chemistry for Designing High Efficiency Thermoelectric Materials. Chem. Mater. *22*, 624–634.

41. de Boor, J. (2021). On the applicability of the single parabolic band model to advanced thermoelectric materials with complex band structures. J. Mater. *7*, 603–611.

42. Bahk, J.H., Bian, Z., and Shakouri, A. (2014). Electron transport modeling and energy filtering for efficient thermoelectric Mg2Si1−xSnx. Phys. Rev. B *89*. 075204.

43. Naithani, H., Müller, E., and de Boor, J. (2022). Developing a two-parabolic band model for thermoelectric transport modelling using Mg 2 Sn as an example. JPhys Energy *4*. 045002.

44. Satyala, N., and Vashaee, D. (2012). Modeling of Thermoelectric Properties of Magnesium Silicide (Mg2Si). J. Electron. Mater. *41*, 1785–1791.

45. Vining, C.B. (1991). A model for the high-temperature transport properties of heavily doped n -type silicon-germanium alloys. J. Appl. Phys. *69*, 331–341.

46. Mao, J., Liu, W., and Ren, Z. (2016). Carrier distribution in multi-band materials and its effect on thermoelectric properties. J. Mater. *2*, 203–211.

47. Young, R.A. (1993). In The Rietveld Method, R.A. Young, ed. (Oxford University Press).

48. Rietveld, H.M. (1969). A profile refinement method for nuclear and magnetic structures. J. Appl. Crystallogr. *2*, 65–71.

49. Imasato, K., Fu, C., Pan, Y., Wood, M., Kuo, J.J., Felser, C., and Snyder, G.J. (2020). Metallic n-Type Mg3Sb2 Single Crystals Demonstrate the Absence of Ionized Impurity Scattering and Enhanced Thermoelectric Performance. Adv. Mater. *32*.

50. Boor, J.D., Dasgupta, T., and Müller, E. (2016). Chapter 5 Thermoelectric Properties of Magnesium Silicide–Based Solid Solutions and Higher Manganese Silicides. In Materials Aspect of Thermoelectricity (CRC Press), pp. 159–218.

51. Borup, K.A., Toberer, E.S., Zoltan, L.D., Nakatsukasa, G., Errico, M., Fleurial, J.-P., Iversen, B.B., and Snyder, G.J. (2012). Measurement of the electrical resistivity and Hall coefficient at high temperatures. Rev. Sci. Instrum. *83*, 123902.

52. Lowhorn, N.D., Wong-Ng, W., Lu, Z.-Q., Martin, J., Green, M.L., Bonevich, J.E., Thomas, E.L., Dilley, N.R., and Sharp, J. (2011). Development of a Seebeck coefficient Standard Reference Material™. J. Mater. Res. *26*, 1983–1992.

53. Lowhorn, N.D., Wong-Ng, W., Zhang, W., Lu, Z.Q., Otani, M., Thomas, E., Green, M., Tran, T.N., Dilley, N., Ghamaty, S., et al. (2009). Round-robin measurements of two candidate materials for a Seebeck coefficient Standard Reference Material™. Appl. Phys. A *94*, 231–234.

54. Wang, H., Bai, S., Chen, L., Cuenat, A., Joshi, G., Kleinke, H., König, J., Lee, H.W., Martin, J., Oh, M.W., et al. (2015). International Round-Robin Study of the Thermoelectric Transport Properties of an n-Type Half-Heusler Compound from 300 K to 773 K. J. Electron. Mater. *44*, 4482–4491.

55. Lenz, E., Edler, F., and Ziolkowski, P. (2013). Traceable Thermoelectric Measurements of Seebeck Coefficients in the Temperature Range from 300 K to 900 K. Int. J. Thermophys. *34*, 1975–1981.

56. Ziolkowski, P., Edler, F., Stiewe, C., Haupt, S., Huang, K., Ryu, B., Park, S., Dasgupta, T., Sahu, P., Taubmann, R., and Müller, E. (2023). Qualification of Fe0.95Co0.05Si2 as a reference material for high temperature measurement of the thermoelectric power factor. Measurement *207*, 112359.

57. Ziolkowski, P., Stiewe, C., de Boor, J., Druschke, I., Zabrocki, K., Edler, F., Haupt, S., König, J., and Mueller, E. (2017). Iron Disilicide as High-Temperature Reference Material for Traceable Measurements of Seebeck Coefficient Between 300 K and 800 K. J. Electron. Mater. *46*, 51–63.

58. Borup, K.A., de Boor, J., Wang, H., Drymiotis, F., Gascoin, F., Shi, X., Chen, L., Fedorov, M.I., Müller, E., Iversen, B.B., and Snyder, G.J. (2015). Measuring thermoelectric transport properties of materials. Energy Environ. Sci. *8*, 423–435.

59. Martin, J., Tritt, T., and Uher, C. (2010). High temperature Seebeck coefficient metrology. J. Appl. Phys. *108*, 121101.

60. Imasato, K., Kang, S.D., and Snyder, G.J. (2019). Exceptional thermoelectric performance in Mg 3 Sb 0.6 Bi 1.4 for low-grade waste heat recovery. Energy Environ. Sci. *12*, 965–971.

61. Tang, Y., Gibbs, Z.M., Agapito, L.A., Li, G., Kim, H.S., Nardelli, M.B., Curtarolo, S., and Snyder, G.J. (2015). Convergence of multi-valley bands as the electronic origin of high thermoelectric performance in CoSb3 skutterudites. Nat. Mater. *14*, 1223–1228. 1412.

62. Perez, C.J., Wood, M., Ricci, F., Yu, G., Vo, T., Bux, S.K., Hautier, G., Rignanese, G.-M., Snyder, G.J., and Kauzlarich, S.M. (2021). Discovery of multivalley Fermi surface responsible for the high thermoelectric performance in Yb 14 MnSb 11 and Yb 14 MgSb 11. Sci. Adv. *7*, eabe9439.

63. Cavassilas, N., Autran, J.L., Aniel, F., and Fishman, G. (2002). Energy and temperature dependence of electron effective masses in silicon. J. Appl. Phys. *92*, 1431–1433.

64. Seeger, K. (2004). Semiconductor Physics (Springer Berlin Heidelberg).

65. Lundstrom, M. (2000). Fundamentals of Carrier Transport (Cambridge University Press).

66. Kittel, C. (2009). Introduction to Solid State Physics Wiley Indi (Wiley).

67. Taylor, J.R. (1997). An Introduction to Error Analysis : The Study of Uncertainties in Physical Measurements (University Science Books).

68. Ziman, J.M. (1996). Electrons and Phonons: The Theory of Transport Phenomena in Solids (Oxford University Press).

69. Rietveld, H.M. (2014). The Rietveld method. Phys. Scr. *89*. 098002.

70. Chelikowsky, J.R., and Cohen, M.L. (1974). Electronic structure of silicon. Phys. Rev. B *10*, 5095–5107.

71. Tserbak, C., Polatoglou, H.M., and Theodorou, G. (1993). Unified approach to the electronic structure of strained Si/Ge superlattices. Phys. Rev. B *47*, 7104–7124.

72. Varshni, Y.P. (1967). Temperature dependence of the energy gap in semiconductors. Physica *34*, 149–154.

73. Ottaviani, G., Reggiani, L., Canali, C., Nava, F., and Alberigi-Quaranta, A. (1975). Hole drift velocity in silicon. Phys. Rev. B *12*, 3318–3329.

74. Grundmann, M. (2010). The Physics of Semiconductors (Springer Berlin Heidelberg).

75. Goyal, G.K., and Dasgupta, T. (2021). Fabrication and testing of Mg2Si1-xSnx based thermoelectric generator module. Mater. Sci. Eng. B *272*, 115338.

76. Camut, J., Ziolkowski, P., Ponnusamy, P., Stiewe, C., Mueller, E., and de Boor, J. (2023). Efficiency Measurement and Modeling of a High-Performance Mg 2 (Si,Sn)-Based Thermoelectric Generator. Adv. Eng. Mater. *25*, 2200776.

77. Nielsen, D., Put, M.V.D., and Fischetti, M. (2021). Investigating the use of HSE Hybrid Functionals to Improve Electron Transport Calculations in Si, Ge, Diamond, and SiC. In 2021 International Conference on Simulation of Semiconductor Processes and Devices (SISPAD) (IEEE)), pp. 133–137.

78. Canali, C., Jacoboni, C., Nava, F., Ottaviani, G., and Alberigi-Quaranta, A. (1975). Electron drift velocity in silicon. Phys. Rev. B *12*, 2265–2284.

79. Li, Z., Graziosi, P., and Neophytou, N. (2021). Deformation potential extraction and computationally efficient mobility calculations in silicon from first principles. Phys. Rev. B *104*, 195201.

80. Gibbs, Z.M., Ricci, F., Li, G., Zhu, H., Persson, K., Ceder, G., Hautier, G., Jain, A., and Snyder, G.J. (2017). Effective mass and Fermi surface complexity factor from ab initio band structure calculations. npj Comput. Mater. *3*, 8.

81. Snyder, G.J., Pereyra, A., and Gurunathan, R. (2022). Effective Mass from Seebeck Coefficient. Adv. Funct. Mater. *32*, 2112772.

82. Goldsmid, H.J., and Sharp, J.W. (1999). Estimation of the thermal band gap of a semiconductor from seebeck measurements. J. Electron. Mater. *28*, 869–872.

83. Seto, J.Y.W. (1975). The electrical properties of polycrystalline silicon films. J. Appl. Phys. *46*, 5247–5254.

84. Lee, P.M. (1964). Electronic Structure of Magnesium Silicide and Magnesium Germanide. Phys. Rev. *135*, A1110–A1114.

85. Liu, X., Zhu, T., Wang, H., Hu, L., Xie, H., Jiang, G., Snyder, G.J., and Zhao, X. (2013). Low Electron Scattering Potentials in High Performance Mg 2 Si 0.45 Sn 0.55 Based Thermoelectric Solid Solutions with Band Convergence. Adv. Energy Mater. *3*, 1238–1244.

86. Shi, G., and Kioupakis, E. (2018). Relativistic quasiparticle band structures of Mg2Si, Mg2Ge, and Mg2Sn: Consistent parameterization and prediction of Seebeck coefficients. J. Appl. Phys. *123*, 085114.

87. Pshenai-Severin, D.A., Fedorov, M.I., and Samunin, A.Y. (2013). The Influence of Grain Boundary Scattering on Thermoelectric Properties of Mg2Si and Mg2Si0.8Sn0.2. J. Electron. Mater. *42*, 1707–1710.

88. Kutorasinski, K., Wiendlocha, B., Tobola, J., and Kaprzyk, S. (2014). Importance of relativistic effects in electronic structure and thermopower calculations for Mg2Si, Mg2Ge, and Mg2Sn. Phys. Rev. B - Condens. Matter Mater. Phys. *89*, 115205.

89. de Boor, J., Berche, A., and Jund, P. (2020). Density of States Effective Mass for p-Type Mg 2 Si–Mg 2 Sn Solid Solutions: Comparison between Experiments and First-Principles Calculations. J. Phys. Chem. C *124*, 14987–14996.

90. Koenig, P., Lynch, D.W., and Danielson, G.C. (1961). Infrared absorption in magnesium silicide and magnesium germanide. J. Phys. Chem. Solids *20*, 122–126.

91. Morris, R.G., Redin, R.D., and Danielson, G.C. (1958). Semiconducting Properties of Mg2Si Single Crystals. Phys. Rev. *109*, 1909–1915.

92. Liu, W., Han, Z., Ji, J., Feng, T., Yang, J., and Zhang, W. (2023). Uplimit (ZT)max and effective merit parameter B* of thermoelectric semiconductors. Mater. Today Phys. *31*, 100989.

93. Liu, W., Zhou, J., Jie, Q., Li, Y., Kim, H.S., Bao, J., Chen, G., and Ren, Z. (2016). New insight into the material parameter B to understand the enhanced thermoelectric performance of Mg2Sn1−x−yGexSby. Energy Environ. Sci. *9*, 530–539.

94. Mitra, K., Goyal, G.K., Rathore, E., Biswas, K., Vitta, S., Mahapatra, S., and Dasgupta, T. (2018). Enhanced Thermoelectric Performance in Mg 2 Si by Functionalized Co-Doping. Phys. Status Solidi *215*, 1700829.

95. Goyal, G.K., Mukherjee, S., Mallik, R.C., Vitta, S., Samajdar, I., and Dasgupta, T. (2019). High Thermoelectric Performance in Mg 2 (Si 0.3 Sn 0.7) by Enhanced Phonon Scattering. ACS Appl. Energy Mater. *2*, 2129–2137.

96. Jayachandran, B., Dasgupta, T., and Singh, A. (2023). A Constant Properties Model for the Performance Estimation in Segmented Thermoelectric Generator Elements and Its Experimental Validation Using an Mg 2 Si 0.3 Sn 0.7 –Bi 2 Te 2.7 Se 0.3 Segmented Leg. ACS Appl. Energy Mater. *6*, 6157–6170.

97. van der Pauw, L.J. (1958). A method of measuring the resistivity and Hall coefficient on lamellae of arbitrary shape. Philips Tech. Rev. *20*, 220–224.

98. de Boor, J., Stiewe, C., Ziolkowski, P., Dasgupta, T., Karpinski, G., Lenz, E., Edler, F., and Mueller, E. (2013). High-Temperature Measurement of Seebeck Coefficient and Electrical Conductivity. J. Electron. Mater. *42*, 1711–1718.

99. de Boor, J., and Müller, E. (2013). Data analysis for Seebeck coefficient measurements. Rev. Sci. Instrum. *84*. 065102.